



Magnetic resonance image reconstruction using trained geometric directions in 2D redundant wavelets domain and non-convex optimization

Bende Ning ^a, Xiaobo Qu ^{a,*}, Di Guo ^b, Changwei Hu ^c, Zhong Chen ^{a,*}

^a Department of Electronic Science, Fujian Provincial Key Laboratory of Plasma and Magnetic Resonance, Xiamen University, Xiamen, 361005, China

^b School of Computer and Information Engineering, Xiamen University of Technology, Xiamen, 361024, China

^c Department of Electrical and Computer Engineering, Duke University, Durham NC 27708, USA

ARTICLE INFO

Article history:

Received 19 April 2013

Revised 3 July 2013

Accepted 21 July 2013

Keywords:

Compressed sensing

Accelerated imaging

MRI

Sparse representation

Non-convex optimization

Directional wavelets

ABSTRACT

Reducing scanning time is significantly important for MRI. Compressed sensing has shown promising results by undersampling the k-space data to speed up imaging. Sparsity of an image plays an important role in compressed sensing MRI to reduce the image artifacts. Recently, the method of patch-based directional wavelets (PBDW) which trains geometric directions from undersampled data has been proposed. It has better performance in preserving image edges than conventional sparsifying transforms. However, obvious artifacts are presented in the smooth region when the data are highly undersampled. In addition, the original PBDW-based method does not hold obvious improvement for radial and fully 2D random sampling patterns. In this paper, the PBDW-based MRI reconstruction is improved from two aspects: 1) An efficient non-convex minimization algorithm is modified to enhance image quality; 2) PBDW are extended into shift-invariant discrete wavelet domain to enhance the ability of transform on sparsifying piecewise smooth image features. Numerical simulation results on *vivo* magnetic resonance images demonstrate that the proposed method outperforms the original PBDW in terms of removing artifacts and preserving edges.

© 2013 Elsevier Inc. All rights reserved.

1. Introduction

Magnetic resonance imaging (MRI) is extensively used to visualize the anatomical or physiological structures of brain, heart, breast and other parts of human bodies. However, slow imaging speed in MRI may result in low spatial resolution in functional MRI [1] or motion artifacts in abdominal MRI [2] and cardiac MRI [3]. The k-space undersampling is one way to accelerate the imaging speed at the expense of introducing aliasing artifacts. Assuming that an image is sparse in a sparsifying transform domain, compressed sensing MRI (CS-MRI) [4] can remove these artifacts by randomly undersampling k-space data and enforcing the reconstructed image to be sparse. This technology has shown promising results in many MRI applications, such as brain imaging [4–8], cardiac imaging [9–13], parametric imaging [14] and catheter tracking [15]. In CS-MRI, the sparsity is usually enforced by minimizing the ℓ_1 norm of transform coefficients [4]. Besides, enforcing low rank structures of MR images also successfully removes aliasing artifacts introduced by undersampling [10,11,13].

Sparsifying transform plays a key role in CS-MRI and sparser representations result in better reconstructions. Conventional CS-

MRI usually use pre-constructed basis or dictionaries [4,16–19], which may not sparsely represent images to be reconstructed. Consequently, artifacts are presented in the reconstruction when k-space data are highly undersampled [20–25]. In contrast, adaptive transforms in CS-MRI will lead to lower reconstruction errors since a sparser representation is learnt from the sampled data [20–22].

The patch-based directional wavelets (PBDW) [22] were recently proposed in CS-MRI to better reconstruct edges than conventional CS-MRI methods. PBDW provide sparser representation of images by estimating geometric directions from a reference image reconstructed using conventional CS-MRI methods. However, artifacts generated in the smooth regions of the reference image (Fig. 1(b)) lead to incorrect geometric directions (Fig. 1(e)) when k-space data are highly undersampled. These artifacts are hard to remove for PBDW as marked in Fig. 1(c) since PBDW cannot sparsify the smooth regions better than conventional sparsifying transform as evidenced in the Section 3.4 of [22]. These artifacts may be viewed as meaningful edges and possibly mislead the diagnosis.

To overcome this limitation of the method proposed in [22], we take the advantage of multiscale decomposition on sparsely representing piecewise smooth features [26]. When the reference image is decomposed into coarse and fine subbands, artifacts in the smooth region are obviously weakened in the coarse subbands (Fig. 2(a)) and two of fine subbands (Figs. 2(b) and (c)). Artifacts in

* Corresponding authors. Tel.: +86 592 2181712; fax: +86 592 2189426.

E-mail addresses: quxiaobo@xmu.edu.cn (X. Qu), chenz@xmu.edu.cn (Z. Chen).

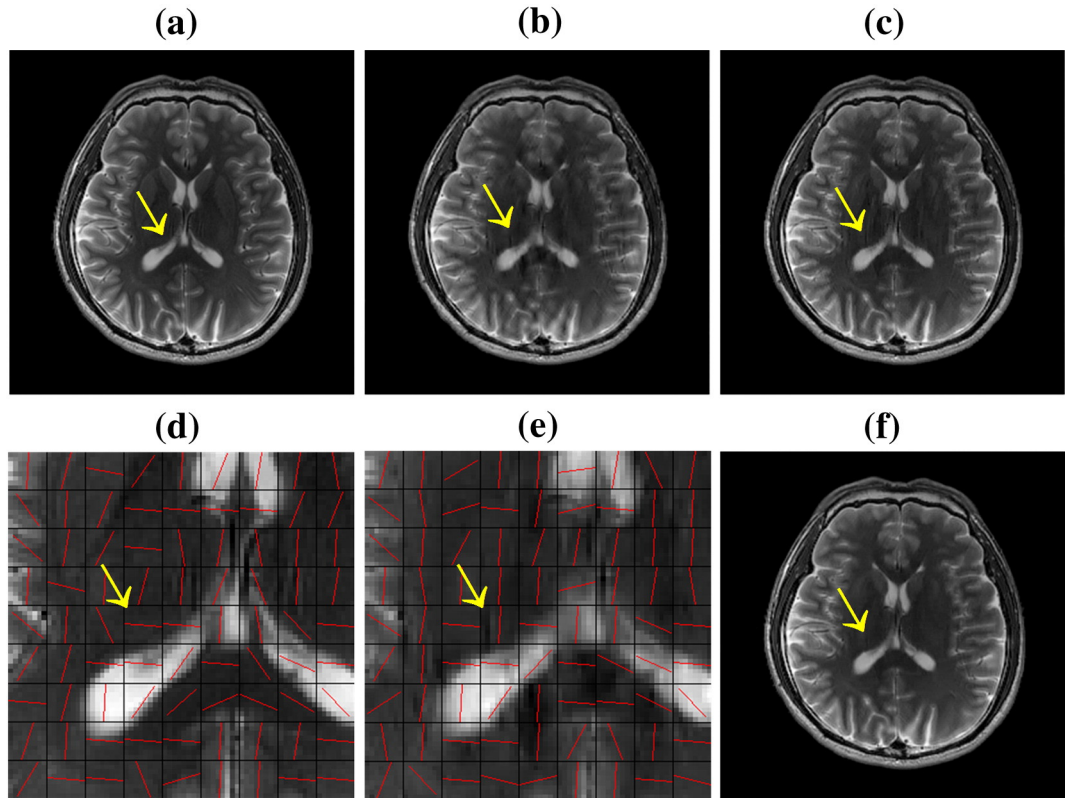


Fig. 1. Reconstructed images from highly undersampled data. (a) fully sampled image; (b) and (c) are reconstructed images using shift-invariant discrete wavelets and PBDW with 30% of fully sampled data, respectively; (d) and (e) are estimated geometric directions from fully sampled image in (a) and reconstructed image in (b) using conventional CS-MRI methods; (f) reconstructed image by the proposed method.

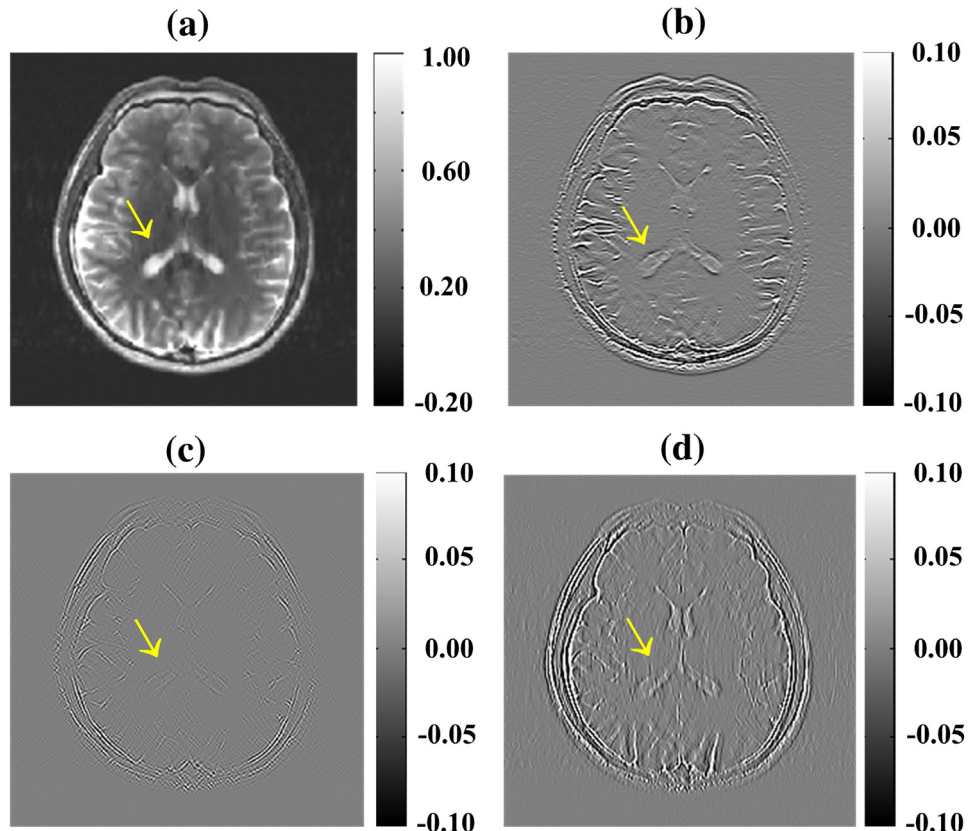


Fig. 2. Decomposed subbands in shift-invariant discrete wavelets domain when decomposition scale is 1. (a) a low frequency subband; (b)–(d) are three high frequency subbands. Note: The source image used in wavelet decomposition is Fig. 1(b), which is also the reference image that geometric directions are estimated from.

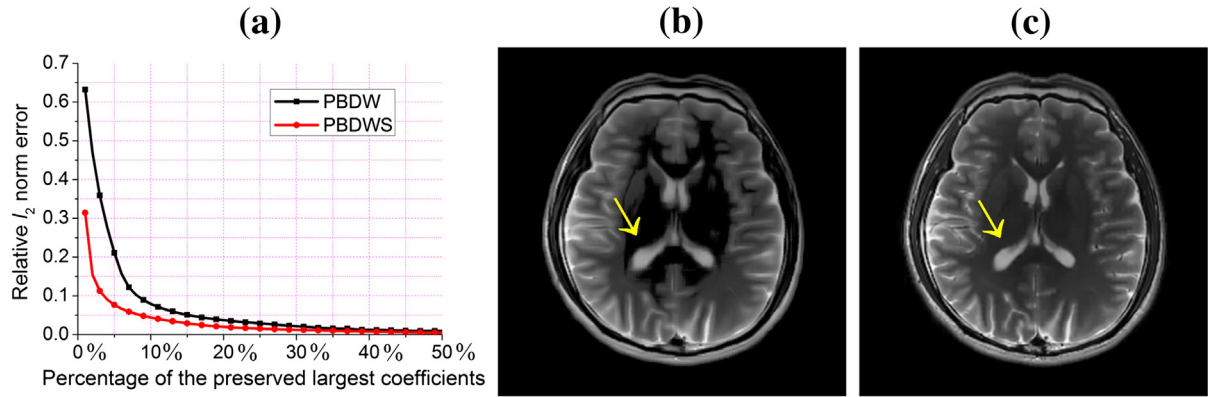


Fig. 3. Sparsity of PBDW and the proposed PBDW in shift-invariant discrete wavelets (PBDWS) domain. (a) Approximation errors versus the percentage of preserved largest coefficients; (b) and (c) are approximated images when 5% preserved largest coefficients are used. Note: Reference image in Fig. 1(b) is used to estimate geometric directions.

the smooth region are mainly observed in a fine subband representing vertical edges (Fig. 2(d)). Weakened pseudo edges will help PBDW to estimate right geometric directions. In addition, applying PBDW in the 2D wavelet subbands will achieve sparser representation of 2D wavelet coefficients since re-transform large magnitude coefficients according to geometric directions will obtain many values close to zero [27,28]. As shown in Fig. 3, a faster decay of approximation error is achieved using the proposed method than the original PBDW. When the 5% largest transform coefficients are preserved, PBDW fail to represent the smooth region while extending it into 2D wavelet domain will significantly improve the representation. Therefore, applying PBDW in the 2D wavelet domain is expected to benefit PBDW removing the artifacts in smooth regions of reconstructed images.

Non-convex optimization with ℓ_p ($0 \leq p < 1$) norm minimization has been proposed to preserve edges in MR image reconstruction from highly undersampled data [29–33] and in image deconvolution [34,35]. For the ℓ_0 norm $\|\alpha\|_0$ which counts the nonzero entries of $\alpha \in \mathbb{R}^N$, a weighted ℓ_1 norm $\|\Lambda\alpha\|_1$ ($\in \mathbb{R}^{N \times N}$) with weights $\Lambda_{i,i} = |\mathbf{z}_i|^{-1}$ and $\Lambda_{i,j} = 0$ ($i \neq j$) mimicks ℓ_0 norm when $|\mathbf{z}_i| \rightarrow |\alpha_i|$ [36]. This implies that ℓ_0 norm $\|\alpha\|_0$ could be viewed as penalizing small magnitude entries of α while encouraging large magnitude entries in image reconstruction. Therefore, minimizing ℓ_0 norm minimization will further suppress the artifacts in smooth regions, shown in Fig. 1(f), which have been weakened in the wavelet domain.

With the reasons stated above, we propose to apply original PBDW in 2D wavelet domain in CS-MRI in this paper. Hopefully, more artifacts will be removed in the undersampled image reconstruction. A shift-invariant discrete wavelet (SIDWT) based on wavelet frame as shown in Fig. 2, is adopted as 2D wavelets which enable fast computation [37] and outperform orthogonal discrete wavelets in reconstructing MR images [18,22,38–40]. The PBDW in the SDIWT domain are denoted as PBDWS in this paper. For the numerical algorithm solving non-convex optimization, a stable and fast numerical algorithm called mean doubly augmented Lagrangian (MDAL) [35], originally solving image deblurring problem, is modified to fit the proposed PBDWS for better MRI reconstruction.

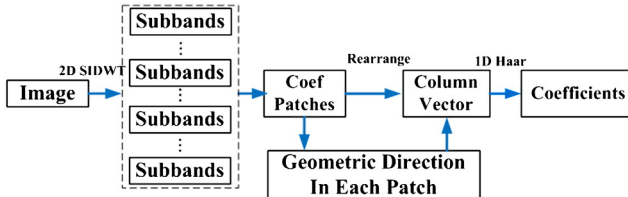


Fig. 4. Flowchart of patch-based directional wavelet in the SIDWT domain.

2. Methods

2.1. L_0 norm minimization for image reconstruction in PBDWS domain

SIDWT is an undecimated wavelet transform since it avoids the subsampling in orthogonal wavelets [26]. Each subband of SIDWT has the same size of the original image. This property benefits analyzing the edges [40]. In addition, redundancy in SIDWT further improves the reconstruction quality [18,22,38–40]. Therefore, SIDWT is adopted as 2D wavelets to sparsify the image in the first step.

In the proposed method, PBDW are performed on each subband of SIDWT as the second step. The flowchart of PBDWS is illustrated in Fig. 4. The geometric direction w_j for the j^{th} patch in subbands of SIDWT is obtained by minimizing S -term approximation error to achieve the sparsity of coefficients [22,27,28] according to

$$w_{j,q} = \arg \min_{\theta_{j,d} \in \Theta} \|\tilde{\mathbf{c}}_{j,d}(\theta_{j,d}, S) - \Psi^T \mathbf{P}(\theta_{j,d}) \mathbf{R}_j \Phi^T \mathbf{x}\|_2^2 \quad (1)$$

where α_j is the operation dividing subbands of $\Phi^T \mathbf{x}$ into patches. $\Theta = \{\theta_1, \theta_2, \dots, \theta_d, \dots, \theta_D\}$ is the set of candidate directions. $\theta_{j,d}$ is the d^{th} candidate direction in the j^{th} patch. $\mathbf{P}(\theta_{j,d})$ is an

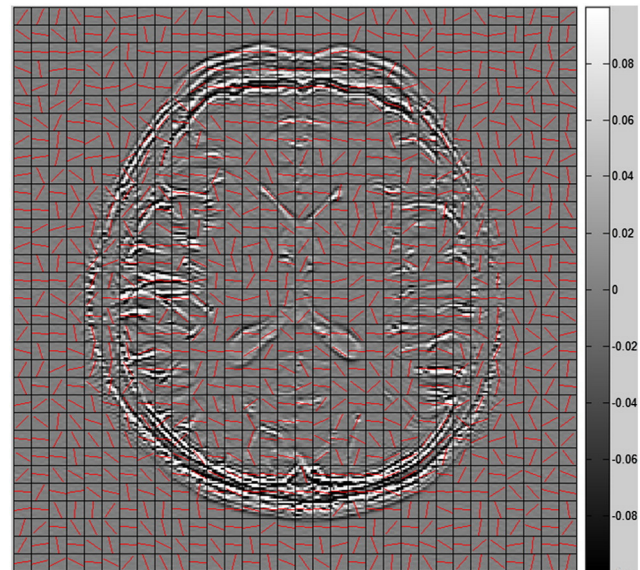


Fig. 5. Geometric directions trained in a SIDWT subband.

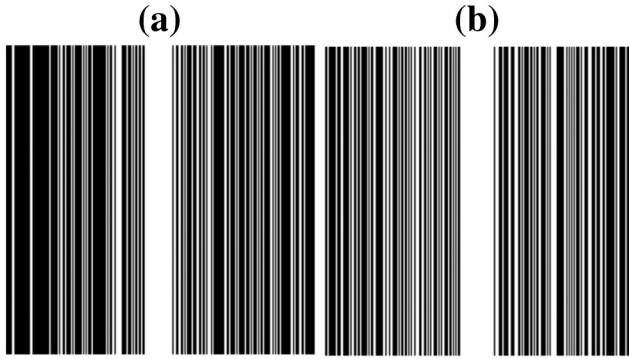


Fig. 6. Two Cartesian sampling patterns. (a) 35% k-space data are sampled; (b) 45% k-space data are sampled.

operation re-arranging pixels according to the direction $\theta_{j,d}$. The notation $\tilde{\mathbf{c}}_j, d(\theta_{j,d}, S)$ denotes the S largest wavelet coefficients of $\Psi^T \mathbf{P}(\theta_{j,d}) \mathbf{R}_j \Phi^T \mathbf{x}$. Estimated directions in one SIDWT subband are shown in Fig. 5.

When the geometric directions of patches are available, 1D Haar transform is performed on the SIDWT coefficients as follows:

$$\mathbf{z} = \begin{bmatrix} \boldsymbol{\alpha}_1 \\ \vdots \\ \boldsymbol{\alpha}_j \\ \vdots \\ \boldsymbol{\alpha}_J \end{bmatrix} = \begin{bmatrix} \Psi^T \mathbf{P}(w_1) \mathbf{R}_1 \\ \vdots \\ \Psi^T \mathbf{P}(w_j) \mathbf{R}_j \\ \vdots \\ \Psi^T \mathbf{P}(w_J) \mathbf{R}_J \end{bmatrix} \Phi^T \mathbf{x} = \mathbf{B}_W \mathbf{x} \quad (2)$$

$$\text{where } \mathbf{B}_W = \begin{bmatrix} \Psi^T \mathbf{P}(w_1) \mathbf{R}_1 \\ \vdots \\ \Psi^T \mathbf{P}(w_j) \mathbf{R}_j \\ \vdots \\ \Psi^T \mathbf{P}(w_J) \mathbf{R}_J \end{bmatrix} \Phi^T.$$

In CS-MRI, the image is commonly reconstructed by minimizing ℓ_1 norm of transform coefficients. The ℓ_0 norm minimization can

reconstruct the images with fewer measurements [29–31]. Therefore, in the PBDWS-based image reconstruction we use minimizing the ℓ_0 norm of transform coefficients instead of ℓ_1 norm minimization as follows:

$$\hat{\mathbf{x}} = \arg \min_{\mathbf{x}} \|\mathbf{B}_W \mathbf{x}\|_0 + \frac{\lambda}{2} \|\mathbf{y} - \mathbf{F}_U \mathbf{x}\|_2^2 \quad (3)$$

where $\mathbf{F}_U = \mathbf{U} \mathbf{F} \in \mathbb{C}^{M \times N}$ denotes the undersampled Fourier transform and \mathbf{y} denotes the acquired k-space data. The terms $\|\mathbf{B}_W \mathbf{x}\|_0$ and $\|\mathbf{y} - \mathbf{F}_U \mathbf{x}\|_2^2$ are used to enforce the sparsity of image \mathbf{x} and data consistency, respectively, while λ balances sparsity and data consistency.

2.2. Numerical algorithm

The ℓ_0 norm term in Eq. (3) is rewritten as follows:

$$\|\mathbf{B}_W \mathbf{x}\|_0 = \left\| \begin{bmatrix} \Psi^T \mathbf{P}(w_1) \mathbf{R}_1 \\ \vdots \\ \Psi^T \mathbf{P}(w_j) \mathbf{R}_j \\ \vdots \\ \Psi^T \mathbf{P}(w_J) \mathbf{R}_J \end{bmatrix} \Phi^T \mathbf{x} \right\|_0 = \left\| \begin{bmatrix} \Psi^T \mathbf{P}(w_1) \mathbf{R}_1 \Phi^T \mathbf{x} \\ \vdots \\ \Psi^T \mathbf{P}(w_j) \mathbf{R}_j \Phi^T \mathbf{x} \\ \vdots \\ \Psi^T \mathbf{P}(w_J) \mathbf{R}_J \Phi^T \mathbf{x} \end{bmatrix} \right\|_0 = \left\| \begin{bmatrix} \boldsymbol{\alpha}_1 \\ \vdots \\ \boldsymbol{\alpha}_j \\ \vdots \\ \boldsymbol{\alpha}_J \end{bmatrix} \right\|_0 \quad (4)$$

where $\boldsymbol{\alpha}_j$ satisfies

$$\boldsymbol{\alpha}_j = \Psi^T \mathbf{P}(w_j) \mathbf{R}_j \Phi^T \mathbf{x}. \quad (5)$$

Alternating direction minimization with augmented Lagrangian method is shown to be fast in solving the ℓ_1 norm minimization problems for CS-MRI [41,42]. An improved algorithm of alternating direction minimization, which is called mean doubly augmented Lagrangian (MDAL) [35], is extended into solving the ℓ_0 norm minimization problem and shown to be stable. Numerical simulations in [35] showed that the MDAL algorithm was superior to penalty decomposition [43] in terms of both efficiency and the quality of the restored image in deconvolution problems. In this paper, MDAL was extended into the proposed PBDWS-based MRI reconstruction.

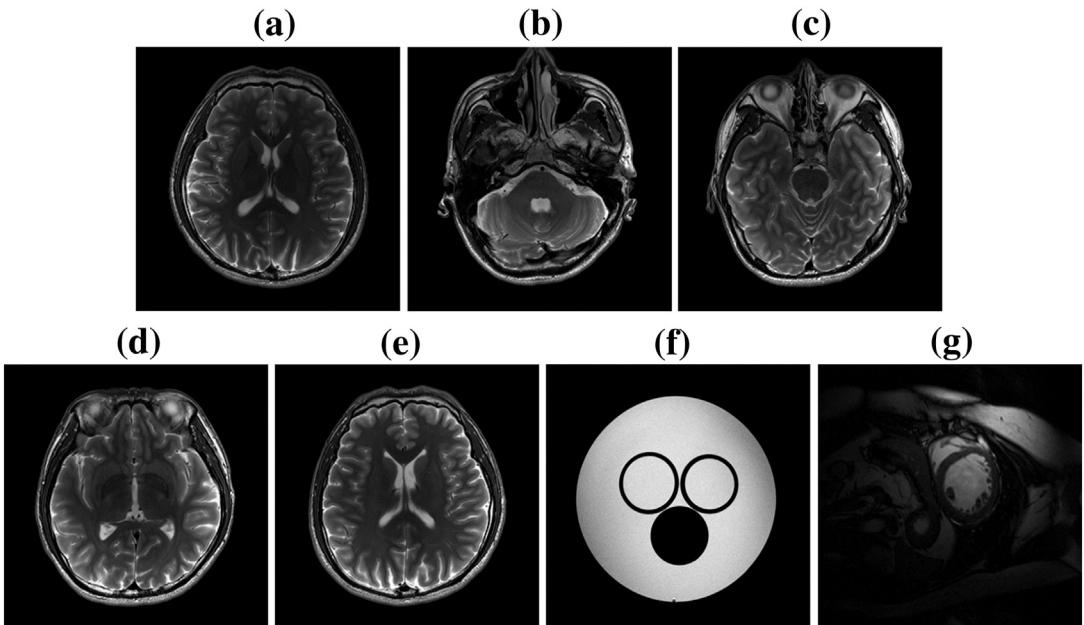


Fig. 7. Fully sampled images used in simulation. (a)–(e) T2 weighted brain images; (f) water phantom image; (g) cardiac image.

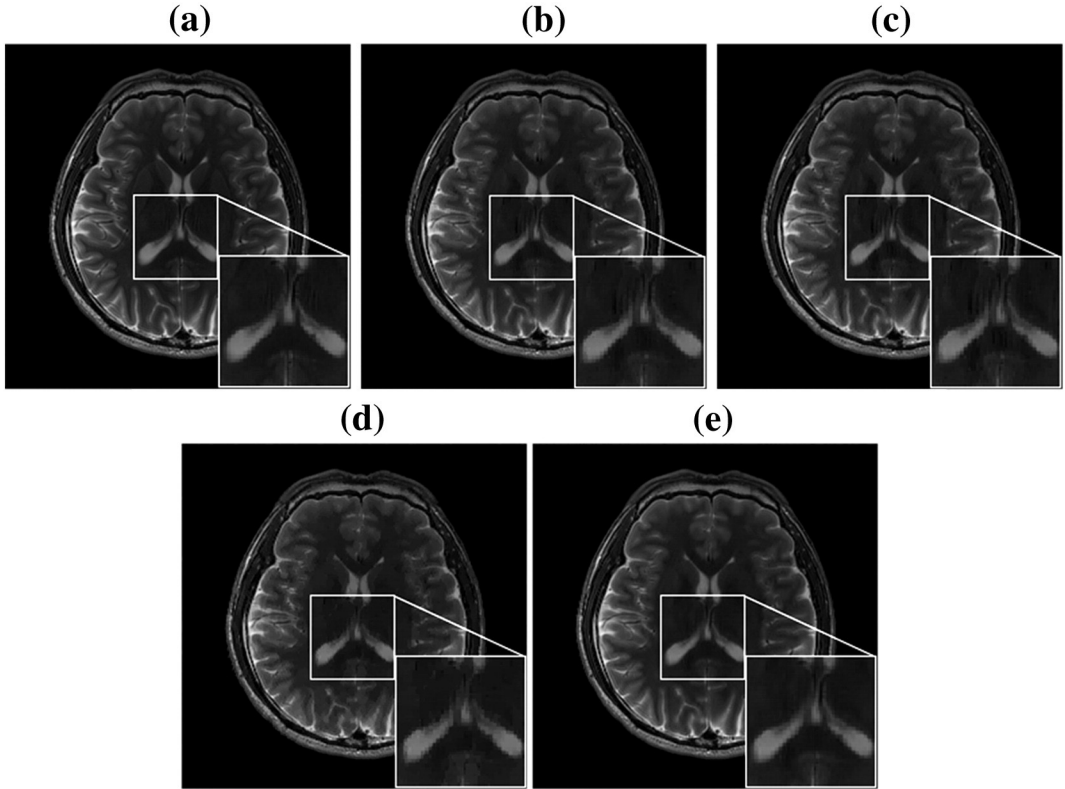


Fig. 8. Reconstructed brain images when 35% k-space data are sampled. (a) the fully sampled image; (b) and (c) are reconstructed images using PBDW with l_1 norm and l_0 norm minimization, respectively; (d) reconstructed image using total variation with homotopic l_0 norm minimization; (e) reconstructed images using PBDWS with l_0 norm minimization.

The MDAL of Eq. (3) is defined as

$$\begin{aligned} L(\mathbf{x}, \boldsymbol{\alpha}, \tilde{\mathbf{v}}, \tilde{\mathbf{x}}, \boldsymbol{\alpha}) = & \min_{\mathbf{x}, \boldsymbol{\alpha}} \frac{\lambda}{2} \|\mathbf{F}_U \mathbf{x} - \mathbf{y}\|_2^2 + \|\boldsymbol{\alpha}\|_0 + \langle \mathbf{v}, \mathbf{B}_W \mathbf{x} - \boldsymbol{\alpha} \rangle \\ & + \frac{\mu}{2} \|\mathbf{B}_W \mathbf{x} - \boldsymbol{\alpha}\|_2^2 + \frac{\gamma}{2} \|\mathbf{x} - \tilde{\mathbf{x}}\|_2^2 + \frac{\gamma}{2} \|\boldsymbol{\alpha} - \tilde{\boldsymbol{\alpha}}\|_2^2 \end{aligned} \quad (6)$$

where μ and γ are two constants, \mathbf{v} is an intermediate variable in iteration, $\tilde{\mathbf{x}}$ and $\tilde{\boldsymbol{\alpha}}$ are the solution of \mathbf{x} and $\boldsymbol{\alpha}$ in last iteration, respectively. Eq. (6) is solved via iteratively solving three sub-problems

$$\begin{cases} \mathbf{x}^{k+1} = \min_{\mathbf{x}} \frac{\lambda}{2} \|\mathbf{F}_U \mathbf{x} - \mathbf{y}\|_2^2 + \frac{\mu}{2} \|\mathbf{B}_W \mathbf{x} - \boldsymbol{\alpha} + \mathbf{v}\|_2^2 + \frac{\gamma}{2} \|\mathbf{x} - \mathbf{x}^k\|_2^2 \\ \boldsymbol{\alpha} = \min_{\boldsymbol{\alpha}} \|\boldsymbol{\alpha}\|_0 + \frac{\mu}{2} \|\mathbf{B}_W \mathbf{x} - \boldsymbol{\alpha} + \mathbf{v}\|_2^2 + \frac{\gamma}{2} \|\boldsymbol{\alpha} - \boldsymbol{\alpha}^k\|_2^2 \\ \mathbf{v}^{k+1} = \mathbf{v}^k + (\mathbf{B}_W \mathbf{x}^{k+1} - \boldsymbol{\alpha}^{k+1}) \end{cases} \quad (7)$$

until the solution converges. Here, we only discuss how to solve the first two sub-problems which are related to the proposed sparsifying

transform PBDWS in CS-MRI. The third sub-problem can be easily solved [35, 43] and is summarized in [Algorithm 1](#).

The first sub-problem in Eq. (7) is solved according to the following normal equation

$$\begin{aligned} & \left(\mu \sum_{j=1}^J \mathbf{R}_j^T \mathbf{P}^T(w_j) \Psi \Psi^T \mathbf{P}(w_j) \mathbf{R}_j + \lambda \mathbf{F}_U^H \mathbf{F}_U + \gamma \right) \mathbf{x}^{k+1} \\ & = \mu \sum_{j=1}^J \mathbf{R}_j^T \mathbf{P}^T(w_j) \Psi(\boldsymbol{\alpha}_j - \mathbf{v}_j) + \lambda \mathbf{F}_U^H \mathbf{y} + \gamma \mathbf{x}^k. \end{aligned} \quad (8)$$

which is simplified as

$$\mathbf{x}^{k+1} = \mathbf{F}^H \left(c \mathbf{I} + \lambda \mathbf{U}^H \mathbf{U} + \gamma \mathbf{I} \right)^{-1} \left(\mu \mathbf{F} \mathbf{s}_{\boldsymbol{\alpha}, \mathbf{v}} + \lambda \mathbf{U}^H \mathbf{y} + \gamma \mathbf{F} \mathbf{x}^k \right). \quad (9)$$

$$\text{where } \mathbf{s}_{\boldsymbol{\alpha}, \mathbf{v}} = \sum_{j=1}^J \mathbf{R}_j^T \mathbf{P}^T(w_j) W(\boldsymbol{\alpha}_j - \mathbf{v}_j).$$

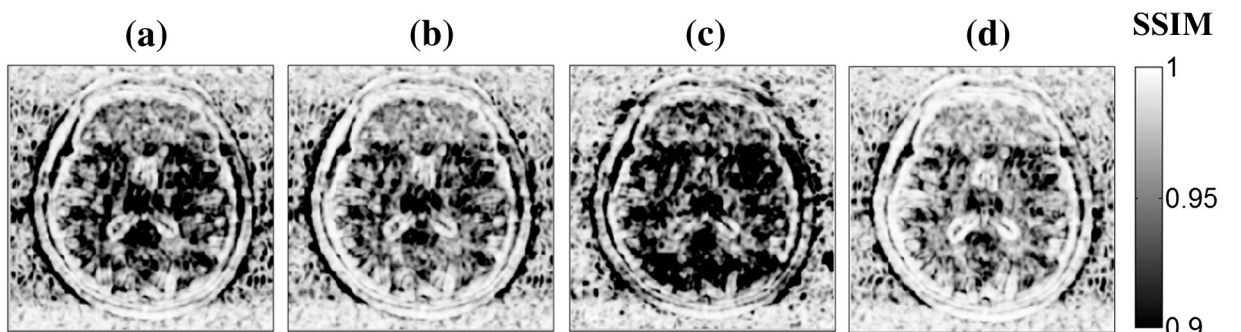


Fig. 9. SSIM metric corresponding to each central pixel. (e)–(g) are the SSIM corresponding to Figs. 8(b)–(e), respectively.

Table 1

Reconstruction errors for Fig. 8(a).

Methods	Images	RLNE	MSSIM
PBDW + l_1 norm	Fig. 8(b)	0.091	0.880
PBDW + l_0 norm	Fig. 8(c)	0.081	0.897
Total variation + l_0 norm	Fig. 8(e)	0.112	0.807
PBDWS + l_0 norm	Fig. 8(d)	0.069	0.970

The second sub-problem in Eq. (7)

$$\boldsymbol{\alpha} = \min_{\boldsymbol{\alpha}} \|\boldsymbol{\alpha}\|_0 + \frac{\mu}{2} \|\mathbf{B}_W \mathbf{x} - \boldsymbol{\alpha} + \mathbf{v}\|_2^2 + \frac{\gamma}{2} \|\boldsymbol{\alpha} - \boldsymbol{\alpha}^k\|_2^2. \quad (10)$$

is solved using hard thresholding

$$\boldsymbol{\alpha}^{k+1} = H_{\mu, \gamma}(\mathbf{B}_W \mathbf{x}^{k+1} + \mathbf{v}^k, \boldsymbol{\alpha}^k). \quad (11)$$

where $H_{\mu, \gamma}$ is defined as

$$(H_{\mu, \gamma}(p, q))_i = \begin{cases} 0, & \text{if } \left| \frac{\mu p_i + \gamma q_i}{\mu + \gamma} \right| < \sqrt{\frac{2}{\mu + \gamma}}. \\ \frac{\mu p_i + \gamma q_i}{\mu + \gamma}, & \text{otherwise} \end{cases} \quad (12)$$

The pseudo-code of the proposed method is summarized in **algorithm 1**. It is worth noting that MDAL takes $\bar{\mathbf{x}}^k = \frac{1}{k+1} \sum_{j=0}^k \mathbf{x}^j$ as output to ensure the convergence of the algorithm [35].

Algorithm 1. Pseudocode for PBDWS-based CS-MRI reconstruction**Initialization:**

Input acquired k-space data \mathbf{y} , the geometric directions $\mathbf{W} = \{w_1, \dots, w_j, \dots, w_M\}$ for all the patches in SIDWT subbands, overlapping factor c and the fast operator \mathbf{F}_U , the Haar wavelet Ψ , the SIDWT Φ , regularization parameter λ , and default parameters $\gamma = 1, \mu = 10^4$ and tolerance of inner loop $\eta = 5 \times 10^{-3}$. The reconstructed image is initialized as $\mathbf{x} = \mathbf{F}_U^H \mathbf{y}$ and other variables are initialized as $\mathbf{v}^0 = 0, \bar{\mathbf{x}}^0 = 0, \boldsymbol{\alpha}^0 = 0$.

Main:While $\bar{\mathbf{x}}^{k+1} - \bar{\mathbf{x}}^k \leq$ is not satisfied, do

- (1) update $\mathbf{x}^{k+1} = \mathbf{F}_U^H (\mu \mathbf{I} + \lambda \mathbf{U}^H \mathbf{U} + \gamma \mathbf{I})^{-1} (\mu \mathbf{F}_{S_{\mathbf{av}}} + \lambda \mathbf{U}^H \mathbf{y} + \gamma \mathbf{F} \mathbf{x}^k);$
- (2) update $\boldsymbol{\alpha}^k: \boldsymbol{\alpha}^{k+1} = H_{\mu, \gamma}(\mathbf{B}_W \mathbf{x}^{k+1} + \mathbf{v}^k, \boldsymbol{\alpha}^k);$
- (3) update $\mathbf{v}: \mathbf{v}^{k+1} = \mathbf{v}^k + (\mathbf{B}_W \mathbf{x}^{k+1} - \boldsymbol{\alpha}^{k+1});$
- (4) update $\bar{\mathbf{x}}^{k+1} = \frac{k+1}{k+2} \bar{\mathbf{x}}^k + \frac{1}{k+2} \mathbf{x}^{k+1};$

End**Output:** $\bar{\mathbf{x}}$ **3. Simulation results****3.1. Simulation setup****3.1.1. Evaluation criteria**

The relative ℓ_2 norm error (RLNE), structural similarity (SSIM) index [44], and signal-to-noise ratio (SNR) [22] are adopted to evaluate the quality of reconstructed image. The expression of RNLE is

$$\text{RLNE}(\hat{\mathbf{x}}) = \frac{\|\hat{\mathbf{x}} - \tilde{\mathbf{x}}\|_2}{\|\tilde{\mathbf{x}}\|_2} \quad (13)$$

It is applied to measure the difference between the fully sampled image $\tilde{\mathbf{x}}$ and the reconstructed image $\hat{\mathbf{x}}$. Lower RLNE indicates the smaller difference between the reconstructed image and the fully sampled image.

SSIM [44] evaluates local reconstruction errors by measuring the similarity between two images in a local window. This criterion has been widely used to measure the image quality when a reference image is available. In our case, the reference image is the fully sampled image. Definition of SSIM is as follows: For two local windows \mathbf{a} and \mathbf{b} , whose size is $G \times G$, the SSIM between them is

$$\text{SSIM}(\mathbf{a}, \mathbf{b}) = \frac{(2\mu_a \mu_b + C_1)(2\sigma_{ab} + C_2)}{(\mu_a^2 + \mu_b^2 + C_1)(\sigma_a^2 + \sigma_b^2 + C_2)} \quad (14)$$

where μ_a is the average of a , μ_b is the average of b , σ_a^2 is the variance of a , σ_b^2 is the variance of b , σ_{ab} is the covariance of a and b , C_1 and C_2 are two variables to stabilize the division with weak denominator. Higher SSIM means the two windows are more similar to each other. Therefore, SSIM criteria corresponding to each central pixel are a useful way to display the local reconstruction errors.

Displaying the SSIM for many images is not convenient. A mean SSIM (MSSIM) of the entire image is a common evaluation of overall image quality [44]. MSSIM is defined as

$$\text{MSSIM}(\mathbf{A}, \mathbf{B}) = \frac{1}{R} \sum_{i=1}^R \text{SSIM}(\mathbf{a}_i, \mathbf{b}_i). \quad (15)$$

where \mathbf{A} and \mathbf{B} are the fully sampled and reconstructed images, respectively; \mathbf{a}_i and \mathbf{b}_i are the image contents at the i^{th} local window, and R is the number of total local windows. In our implementation, R equals to the number of pixels of an image meaning that each pixel is the center of a local window. Higher MSSIM values indicate stronger detail preservation in reconstruction.

3.1.2. Datasets and sampling patterns

In simulation, variable Cartesian sampling patterns in Fig. 6 are adopted to undersample the k-space data. Images used in simulation include T2 weighted brain images (Figs. 7(a)–(e)), a water phantom image (Fig. 7(f)) and a cardiac image (Fig. 7(g)). The brain images (size

Table 2

Reconstruction errors for Figs. 7(b)–(e).

Methods	Images		Fig. 7(b)		Fig. 7(c)		Fig. 7(d)		Fig. 7(e)	
	RLNE	MSSIM	RLNE	MSSIM	RLNE	MSSIM	RLNE	MSSIM	RLNE	MSSIM
PBDW + l_1 norm	0.104	0.920	0.104	0.921	0.095	0.920	0.052	0.732		
PBDW + l_0 norm	0.096	0.927	0.094	0.931	0.082	0.935	0.051	0.741		
Total variation + l_0 norm	0.130	0.909	0.136	0.890	0.112	0.911	0.059	0.710		
PBDWS + l_0 norm	0.089	0.944	0.089	0.940	0.075	0.949	0.038	0.910		

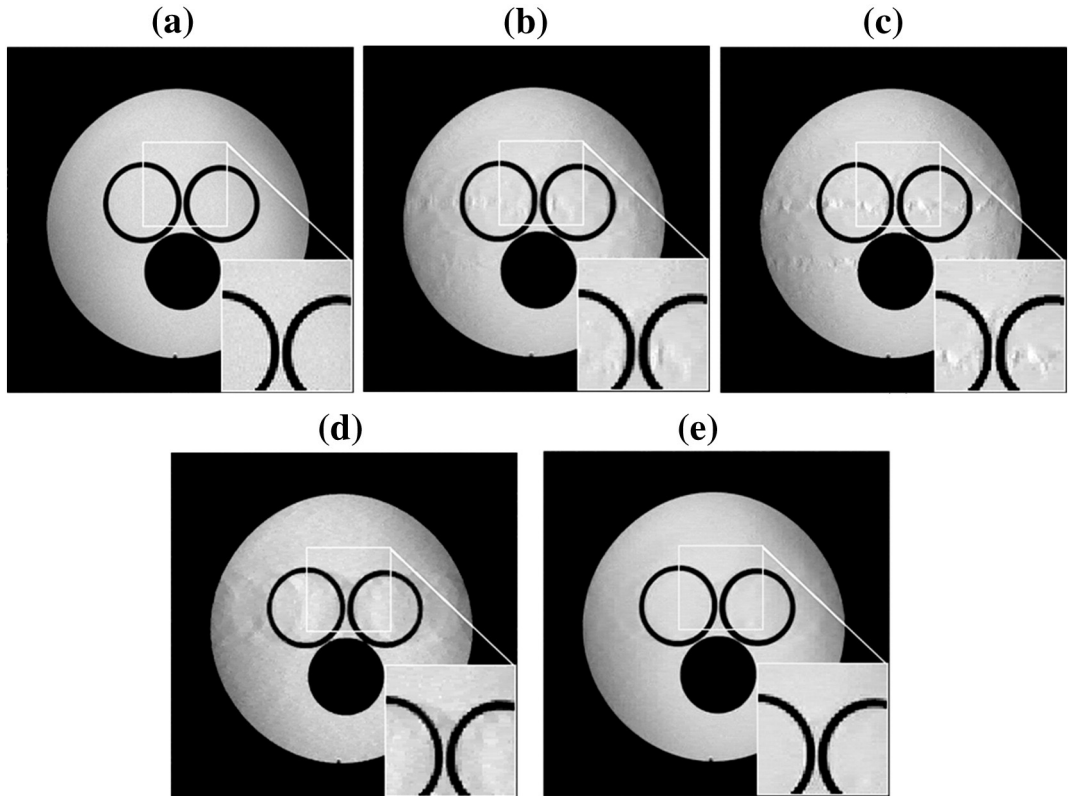


Fig. 10. Reconstructed water phantom images when 35% k-space data are sampled. (a) the fully sampled image; (b) and (c) are reconstructed images using PBDW with l_1 norm and l_0 norm minimization, respectively; (d) reconstructed image using total variation with homotopic l_0 norm minimization; (e) reconstructed images using PBDWS with l_0 norm minimization.

256 × 256) shown in Figs. 7(a)–(e) are acquired from a healthy volunteer at a 3 T Siemens Trio Tim MRI scanner using the T2-weighted turbo spin echo sequence (TR/TE = 6100/99 ms, 220 × 220 mm field of view, 3 mm slice thickness). The water phantom image (size

256 × 256) shown in Fig. 7(f) is acquired at 7 T Varian MRI system (Varian, Palo Alto, CA, USA) with the spin echo sequence (TR/TE = 2000/100 ms, 80 × 80 mm field of view, 2 mm slice thickness). The cardiac image in Fig. 7(g) is downloaded from [45].

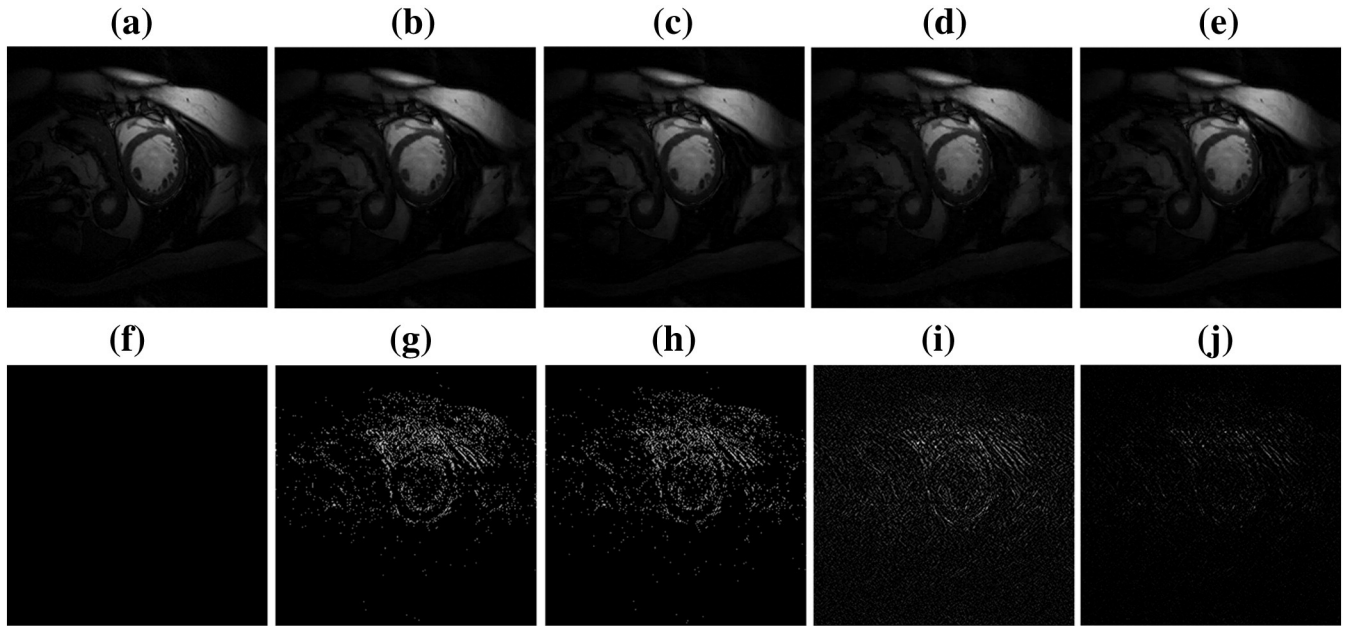


Fig. 11. Reconstructed cardiac images when 45% k-space data are sampled. (a) the fully sampled image; (b) and (c) are reconstructed images using PBDW with l_1 norm and l_0 norm minimization, respectively; (d) reconstructed image using total variation with homotopic l_0 norm minimization; (e) reconstructed images using PBDWS with l_0 norm minimization; (f)–(j) are the difference images between fully sampled MR image and (a)–(e).

Table 3

Reconstruction errors for Figs. 10 and 11.

Methods	Images			
	Fig. 10		Fig. 11	
	RLNE	MSSIM	RLNE	MSSIM
PBDW + l_1 norm	0.052	0.732	0.091	0.841
PBDW + l_0 norm	0.051	0.741	0.094	0.842
Total variation + l_0 norm	0.059	0.710	0.093	0.837
PBDWS + l_0 norm	0.038	0.910	0.082	0.920

3.2. Simulations on in vivo and phantom images

To demonstrate the performance of the proposed method, PBDWS with ℓ_0 norm minimization is compared with original PBDW with ℓ_1 norm minimization [22] and total variation with homotopic ℓ_0 norm minimization [30]. To estimate the geometric directions [22], we use SIDWT-based reconstructed image as a guide image. Regularization parameter λ for PBDW and PBDWS is set as 10^6 . The regularization parameter is 10^5 for homotopic ℓ_0 norm minimization. All simulations are performed on an Intel Core 2 Duo CPU at 3.0 GHz and 2 GB memory.

Reconstructed brain images using 35% of k-space data of Fig. 7(a) is shown in Fig. 8. With ℓ_1 norm minimization, the original PBDW fails to remove the artifacts shown in Fig. 8(b). When we use ℓ_0 norm minimization, these artifacts are slightly better suppressed as shown in Fig. 8(c). Total variation with homotopic ℓ_0 norm minimization method successfully suppressed the artifacts

but introduced stair-case artifacts as shown in Fig. 8(d). Combing PBDWS with ℓ_0 norm minimization, the proposed method significantly suppresses the artifacts and preserves the edges in Fig. 8(e).

SSIM criteria, measuring the local reconstruction errors and corresponding to each central pixel, are evaluated in Fig. 9. It shows that higher SSIM is achieved in most image regions using the proposed method than other methods. This implies that the reconstructed image using the proposed method is more consistent to the fully sampled image.

Besides the visual inspection and local reconstruction errors evaluation, global reconstruction errors, RLNEs and MSSIMs are measured in Table 1, showing that the proposed PBDWS achieves the lowest RLNEs and highest MSSIMs among all the compared methods. This observation is consistent to criteria comparison in Table 2, which is evaluated on reconstruction of other four T2-weighted brain images when 35% of k-space data are sampled.

We also verify the performance of different methods using water phantom and cardiac images. The sampling patterns shown in Figs. 6(a) and (b) are used for water phantom and cardiac images, respectively. For the phantom data, the proposed method achieves the best resolution among all the methods as shown in Fig. 10. For the cardiac image shown in Fig. 11, most image features are obtained by the proposed method. The lowest reconstruction errors RLNEs and highest MSSIMs are achieved by the proposed method for the two datasets as shown in Table 3.

In summary, visual inspections in Figs. 8, 10, and 11 and reconstruction errors in Tables 1–3 demonstrate that PBDWS with ℓ_0 norm minimization outperforms other methods.

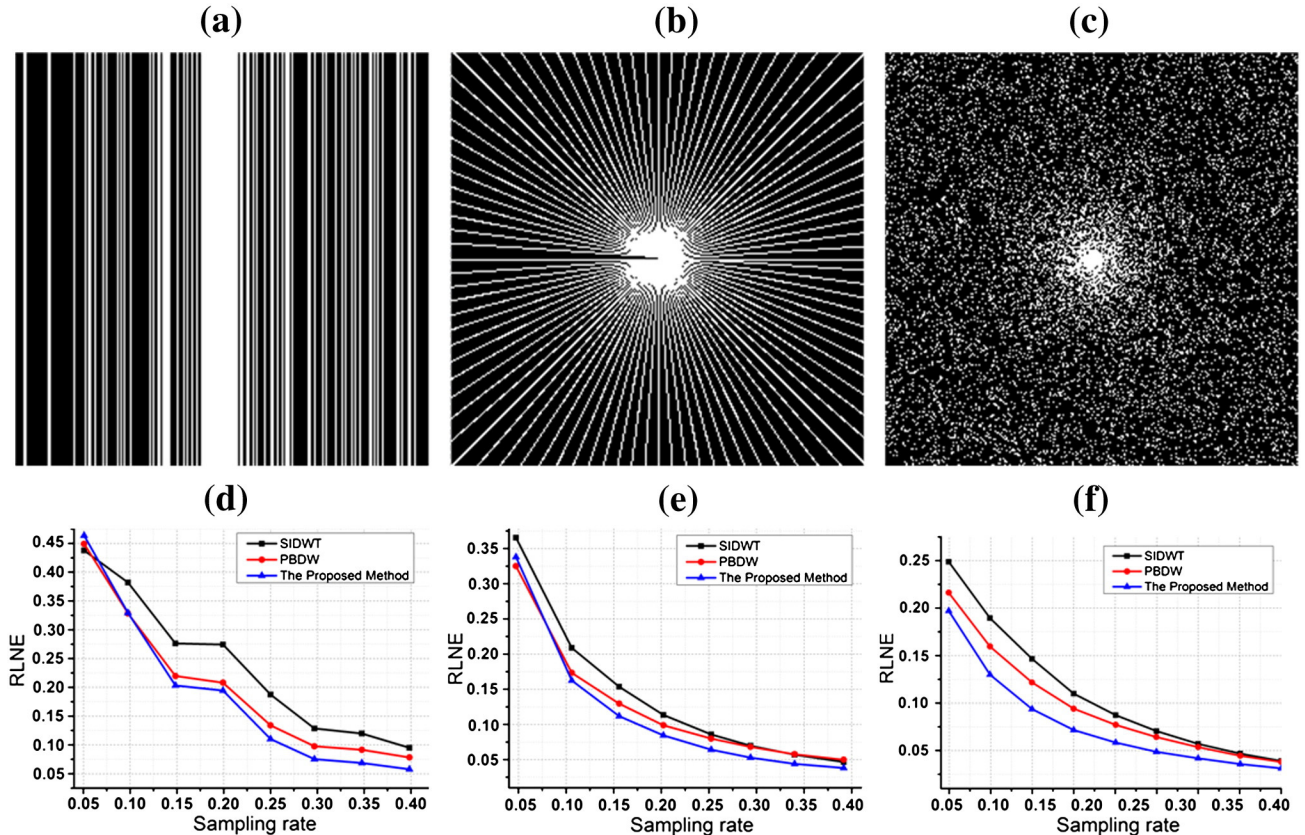


Fig. 12. Reconstruction errors under different sampling patterns. (a)–(c) are Cartesian, radial and 2D undersampling patterns; (d)–(f) are reconstruction errors corresponding to undersampling patterns in (a)–(c), respectively.

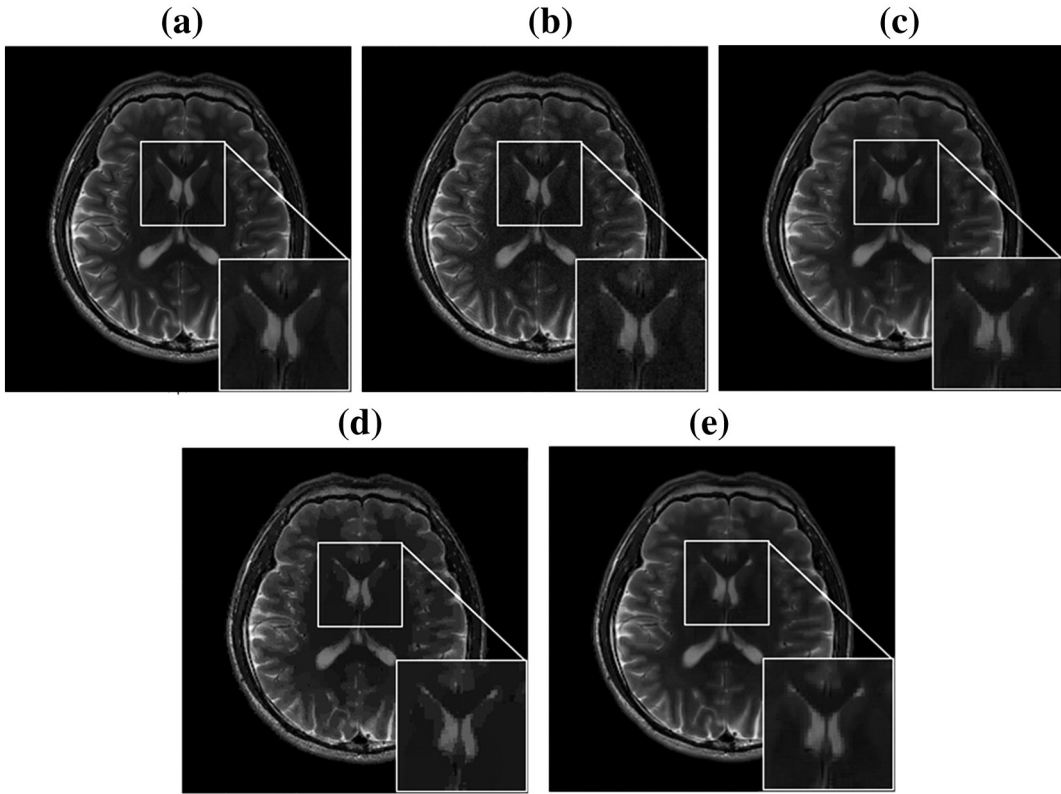


Fig. 13. Comparison on reconstructed images for noise-added data. (a) and (b) are fully sampled image without and with added noise, respectively; (c) reconstructed image using PBDW with l_1 norm minimization; (d) reconstructed image using total variation with homotopic l_0 norm minimization; (e) reconstructed images using PBDWS with l_0 norm minimization.

4. Discussion

4.1. Different undersampling patterns

Reconstruction errors for different undersampling patterns are evaluated in Fig. 12. When the sampling rate is larger than 0.25 for radial sampling as shown in Fig. 12(e) and sampling rate is larger than 0.30 for the fully 2D random sampling as shown in Fig. 12(f), the PBDW cannot maintain the improvement over conventional CS-MRI methods, which is also observed in [25]. But the proposed method overcomes this limitation successfully. Consistent improvement using the proposed method over traditional CS-MRI methods is observed in Fig. 12 when the RLNE is larger than 0.05. These observations imply that the proposed method is robust to sampling patterns.

4.2. Handling noise-added data

To demonstrate the performance with additive noise using the proposed method, a Gaussian white noise with variance $\sigma^2 = 0.20$ was added into real and imaginary parts of original k-space data, respectively. We employed Cartesian sampling shown in Fig. 6(b) to

acquire 45% of the full data. In simulation, while maintaining $\text{SNR} \geq 15$ in the reconstructed images, the choice of regularization parameters for different methods is optimized to suppress most of the noise as well as achieve the lowest RLNEs.

The regularization parameter λ is set as 5×10^3 for PBDW with ℓ_1 norm minimization, $\lambda = 9 \times 10^2$ for the proposed PBDWS with ℓ_0 norm minimization, and the regularization parameter is 10^{-1} for homotopic ℓ_0 norm minimization. For the noise-added image in Fig. 13(b), better noise suppressing and sharper textures or edges are achieved using the proposed method (Fig. 13(e)) than using other methods (Figs. 13(c) and (d)). The proposed method obtained the lowest RLNEs and highest SNRs as shown in Table 4. These results

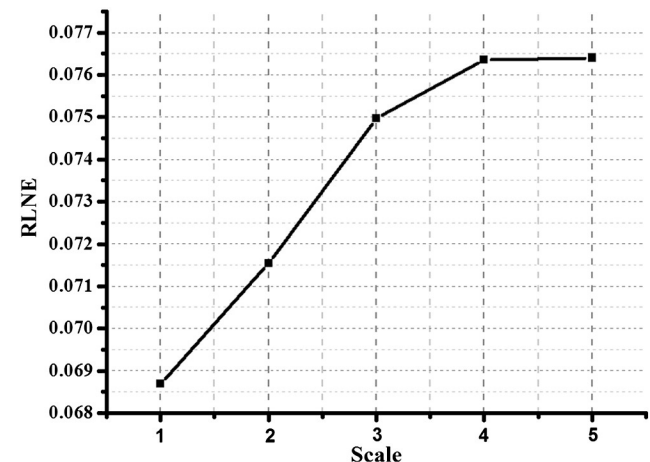


Fig. 14. Reconstruction errors versus decomposition scale of SIDWT.

Table 4
Reconstruction errors for noise-added data.

Methods	Images	RLNE	MSSIM	SNR
Noise added image	Fig. 13(b)	0.095	0.800	10.9
PBDW + l_1 norm	Fig. 13(c)	0.113	0.882	30.6
Total variation + l_0 norm	Fig. 13(d)	0.124	0.871	25.5
PBDWS + l_0 norm	Fig. 13(e)	0.087	0.960	35.3

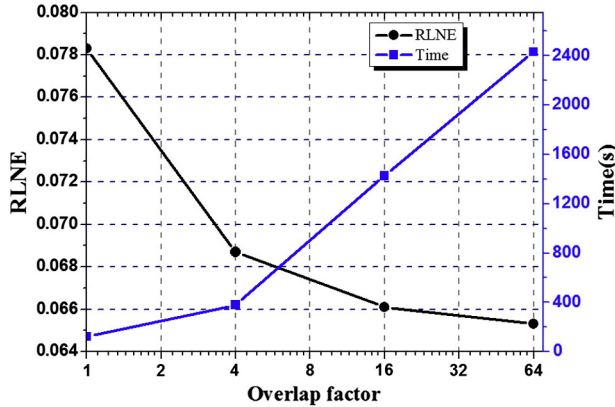


Fig. 15. Computation time and reconstruction errors versus overlap factor.

demonstrate that the proposed method has advantages in preserving the textures or edges for the data with noise.

4.3. Decomposition scales

The optimal decomposition scales of SIDWT are tested. Fig. 14 shows that the reconstruction error increases as the number of decomposition scales grows. The lowest reconstruction error is obtained when decomposition scale is 1. The reason may be that one scale SIDWT filters out the aliasing artifacts introduced by undersampling. However, further increasing the scales results in smoother edges that does not help finding the geometric direction and improving the sparsity in PBDW.

4.4. Overlap factor

Overlap factor is chosen as 4 to tradeoff between computation and reconstruction error. Theoretically, the computational complexity of one forward/inverse PBDWS is proportional to the overlap factor c . Computation time is tested under different overlap factors. As shown in Fig. 15, RLNEs decrease as overlap factor grows. When overlap factor is larger than 4, RLNE decreases slowly. Reduction of RLNE is at the cost of longer computation time. This suggests that overlap factor 4 is optimal in our simulation.

4.5. Convergence of the algorithm

The convergence of the proposed method is empirically tested. Fig. 16(a) is used for the experiment. The reference [35] suggests to test the convergence of MDAL by plotting the evolution of $\frac{\|\bar{x}^k - \bar{x}^{k-1}\|_2}{\|\bar{z}\|_2}$ where \bar{x}^k and \bar{x}^{k-1} are reconstructed image, and \bar{z} is the zero

Table 5
Computation time of different reconstruction methods (unit: seconds).

Methods	Images			
	Fig. 7(b)	Fig. 7(c)	Fig. 7(d)	Fig. 7(e)
PBDW + l_1 norm	351	397	371	373
PBDWS + l_0 norm	358	390	393	337
Total variation + l_0 norm	379	385	373	382

Note: All the methods are carried out until their RLNEs stabilize. The CPU time is averaged by repeating the same simulation 5 times.

filling undersampled magnetic resonance image. The cure in Fig. 16(a) shows that $\frac{\|\bar{x}^k - \bar{x}^{k-1}\|_2}{\|\bar{z}\|_2}$ decreases with iterations. As the iterations increased, the solution progressively approaches the fully sampled as shown in Fig. 16(b). The objective function decreases and gradually stabilizes when the computation time increases as shown in Fig. 16(c). These observations indicate that MDAL converges in the proposed method.

4.6. Computation time

Once geometric directions were estimated from a guide image, the computational complexity of PBDW is $O(cN)$, which is proportional to the overlap factor c of PBDW and the number of pixels N in one image [22]. The computational complexity of PBDWS is $O(c'M)$ where c' is the overlap factor of PBDWS and M is the number of wavelet coefficients in all SIDWT subbands. In typical setting of the proposed method, $c' = \frac{1}{4}c$ and $M = 4N$. Therefore, the PBDWS has the same computational complexity of PBDW with typical overlap factor 16 [22]. The computation time of these methods is summarized in Table 5, which shows that the proposed method can reach lower RLNEs with nearly the same time of PBDW and this time is about 4 times that of conventional SIDWT-based reconstruction.

4.7. Regularization parameters

How to choose the regularization parameters is discussed in this section. Following the principle of maximum likelihood estimation (MLE) [42], regularization parameter λ should be proportional to the inverse of noise variance σ^2 . If the data are free of noise, λ should be as large as possible. In our cases, $\lambda = 10^6$ is large enough to achieve the optimal reconstruction for all the used imaging data without additive noise.

For the noise-added data, regularization parameter λ is crucial to minimize reconstruction errors and maintaining SNRs. From the aspect of MLE [42], a smaller λ penalizes the noise more heavily. The effect of λ values on reconstruction is studied in Fig. 17. It shows that

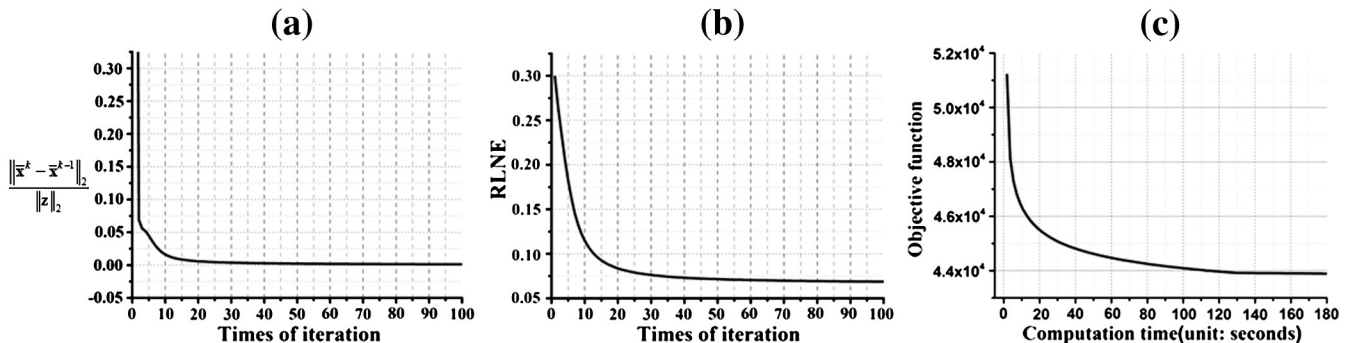


Fig. 16. Empirical convergence of the MDAL algorithm. (a) The decay curve of increments of reconstructed images in iterations; (b) reconstruction errors in iterations; (c) objective function versus computation time.

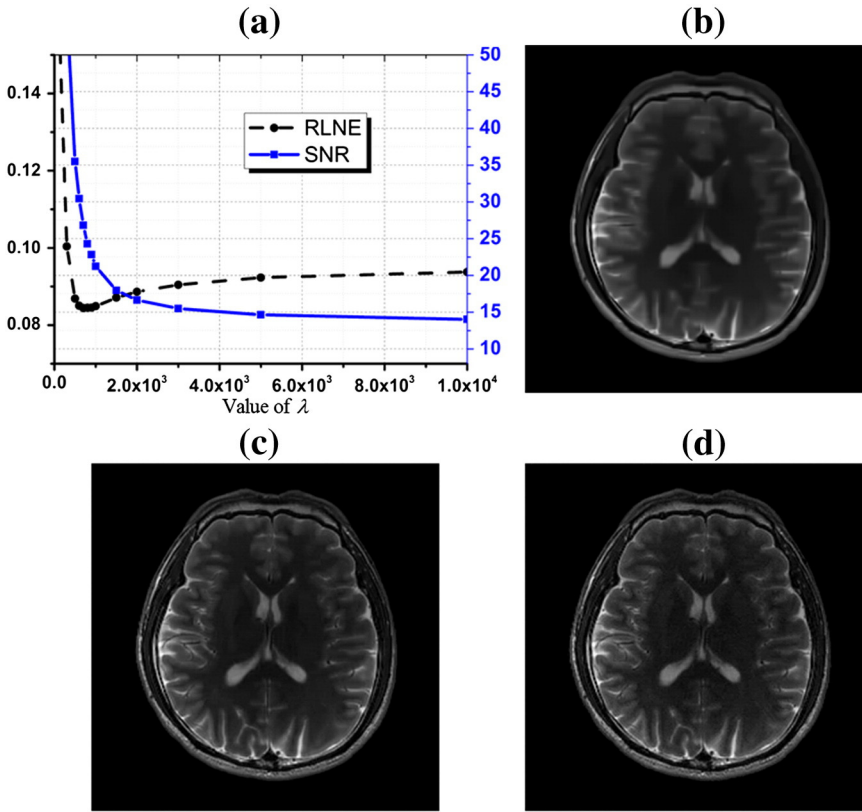


Fig. 17. Effect of regularization parameter λ for reconstruction of brain image with added noise using the proposed method. (a) The RLNEs and SNRs against the regularization parameter λ when 45% k-space data are sampled; (b)–(c) are reconstructed images with $\lambda = 200, 900, 5000$, respectively.

a small λ (5×10^2) results in over-smoothed image while a large λ ($\lambda > 5 \times 10^3$) will introduce residual noise in image. Among the values we tested in this experiment, λ between $[5 \times 10^2, 5 \times 10^3]$ appears to be optimal as suggested with nicely low reconstruction errors and high SNRs.

5. Conclusions

In this work, performance of PBDW-based undersampled magnetic resonance image reconstruction is improved by minimizing the ℓ_0 norm of transform coefficients and extending PBDW into 2D shift-invariant discrete wavelets domain. Image edges are better preserved and the artifacts are better removed than the original PBDW with ℓ_1 norm minimization. The proposed method is observed to be robust to sampling patterns. A mean doubly augmented Lagrangian algorithm makes the solution progressively approach the fully sampled image in iterations. Our future work is combining the proposed method with spread spectrum MRI [46,47], which may reduce the coherence between sampling matrix and sparsifying transform leading to potential reduction of reconstruction errors. In addition, applying other adaptive sparsifying transforms [48,49] and combining them with PBDWS in MR image reconstruction are worth investigating.

Acknowledgments

The authors thank Dr. Bingwen Zheng for valuable suggestions. The authors also sincerely thank Drs. Michael Lustig, Joshua Trzasko, Gabriel Peyre, Junfeng Yang, Yin Zhang, Wotao Yin, Jong Chul Ye and Richard Baraniuk for sharing their codes and/or data. This work was partially supported by NNSF of China (61201045, 11174239 and 10974164), Fundamental Research Funds for the Central Universities

(No. 2013SH002), Open Fund from Key Lab of Digital Signal and Image Processing of Guangdong Province (54600321) and Scientific Research Foundation for the Introduction of Talent at Xiamen University of Technology (90030606).

References

- [1] Hu YL, Glover GH. Increasing spatial coverage for high-resolution functional MRI. *Magn Reson Med* 2009;61:716–22.
- [2] Yang RK, Roth CG, Ward RJ, deJesus JO, Mitchell DG. Optimizing abdominal MR imaging: approaches to common problems. *Radiographics* 2010;30:185–99.
- [3] Finn JP, Nael K, Deshpande V, Ratib O, Laub G. Cardiac MR imaging: state of the technology. *Radiology* 2006;241:338–54.
- [4] Lustig M, Donoho D, JM Pauly. Sparse MRI: the application of compressed sensing for rapid MR imaging. *Magn Reson Med* 2007;58:1182–95.
- [5] Ye JC, Tak S, Han Y, Park HW. Projection reconstruction MR imaging using FOCUS. *Magn Reson Med* 2007;57:764–75.
- [6] Block KT, Uecker M, Frahm J. Undersampled radial MRI with multiple coils. Iterative image reconstruction using a total variation constraint. *Magn Reson Med* 2007;57:1086–98.
- [7] Miao J, Guo W, Narayan S, Wilson DL. A simple application of compressed sensing to further accelerate partially parallel imaging. *Magn Reson Med* 2013; 31:75–85.
- [8] Fang S, Ying K, Zhao L, Cheng JP. Coherence regularization for SENSE reconstruction with a nonlocal operator (CORNOL). *Magn Reson Med* 2010; 64:1414–26.
- [9] Camper U, Boesiger P, Kozerke S. Compressed sensing in dynamic MRI. *Magn Reson Med* 2008;59:365–73.
- [10] Lingala SG, Yue H, DiBella E, Jacob M. Accelerated dynamic MRI exploiting sparsity and low-rank structure: k-t SLR. *IEEE Trans Med Imaging* 2011;30: 1042–54.
- [11] Zhao B, Haldar JP, Christodoulou AG, Liang ZP. Image reconstruction from highly undersampled (k, t)-space data with joint partial separability and sparsity constraints. *IEEE Trans Med Imaging* 2012;31:1809–20.
- [12] Liang D, DiBella EVR, Chen RR, Ying L. k-t ISD: dynamic cardiac MR imaging using compressed sensing with iterative support detection. *Magn Reson Med* 2012;68: 41–53.
- [13] Xie G, Feng X, Christodoulou AG, Weng D, Liu X, Qiu B. High resolution dynamic cardiac MRI using partial separability of spatiotemporal signals with a novel sampling scheme. *Magn Reson Imaging* 2012;31:529–37.

- [14] Doneva M, Bornert P, Eggers H, Stehning C, Senegas J, Mertins A. Compressed sensing reconstruction for magnetic resonance parameter mapping. *Magn Reson Med* 2010;64:1114–20.
- [15] MacDonald ME, Stafford RB, Yerly J, Andersen LB, McCreary CR, Frayne R. Accelerated passive MR catheter tracking into the carotid artery of canines. *Magn Reson Imaging* 2013;31:120–9.
- [16] Qu X, Zhang W, Guo D, Cai C, Cai S, Chen Z. Iterative thresholding compressed sensing MRI based on contourlet transform. *Inverse Probl Sci En* 2010;18: 737–58.
- [17] Kim DH, Gho SM, Nam Y, Zho SY, Kim EY. Three dimension double inversion recovery gray matter imaging using compressed sensing. *Magn Reson Imaging* 2010;28:1395–402.
- [18] Guerquin-Kern M, Haeberlin M, Pruessmann KP, Unser M. A fast wavelet-based reconstruction method for magnetic resonance imaging. *IEEE Trans Med Imaging* 2011;30:1649–60.
- [19] DiBella EVR, Chen LY, Schabel MC. Reconstruction of dynamic contrast enhanced magnetic resonance imaging of the breast with temporal constraints. *Magn Reson Imaging* 2010;28:637–45.
- [20] Ravishankar S, Bresler Y. MR image reconstruction from highly undersampled k-space data by dictionary learning. *IEEE Trans Med Imaging* 2011;30:1028–41.
- [21] Liu Q, Wang S, Yang K, Luo J, Zhu Y, Liang D. Highly undersampled magnetic resonance image reconstruction using two-level Bregman method with dictionary updating. *IEEE Trans Med Imaging* 2013;32:1290–301.
- [22] Qu X, Guo D, Ning B, Hou Y, Lin Y, Cai S, Chen Z. Undersampled MRI reconstruction with patch-based directional wavelets. *Magn Reson Imaging* 2012;30:964–77.
- [23] Du H, Lam F. Compressed sensing MR image reconstruction using a motion-compensated reference. *Magn Reson Imaging* 2012;30:954–63.
- [24] Chen Y, Hager W, Huang F, Phan D, Ye X, Yin W. Fast algorithms for image reconstruction with application to partially parallel MR imaging. *SIAM J Imaging Sci* 2012;5:90–118.
- [25] Lin Q, Guo W, Fu X, Ding X, Huang Y. MR image reconstruction by patch-based sparse representation. *J Theor Appl Inf Technol* 2013;49:107–12.
- [26] Mallat S. A wavelet tour of signal processing. San Diego: Academic Press; 1998.
- [27] Peyre G, Mallat S. Surface compression with geometric bandelets. *ACM Trans Graphic* 2005;24:601–8.
- [28] Le Pennec E, Mallat S. Sparse geometric image representations with bandelets. *IEEE Trans Image Process* 2005;14:423–38.
- [29] Chartrand R. Fast algorithms for nonconvex compressive sensing: MRI reconstruction from very few data. In: Stanley Reeves, editor. 2009 IEEE International Symposium on Biomedical Imaging: from nano to macro-ISBI'09. Boston, MA: IEEE Computer Society; 2009. p. 262–5.
- [30] Trzasko J, Manduca A. Highly undersampled magnetic resonance image reconstruction via homotopic l_0 -minimization. *IEEE Trans Med Imaging* 2009; 28:106–21.
- [31] Qu X, Cao X, Guo D, Hu C, Chen Z. Compressed sensing MRI with combined sparsifying transforms and smoothed l_0 norm minimization. In: Nasser Kehtarnavaz, editor. The 35th International Conference on Acoustics, Speech, and Signal Processing-ICASSP'10. Dallas, Texas, USA: IEEE; 2010. p. 626–9.
- [32] Majumdar A, Ward RK. An algorithm for sparse MRI reconstruction by Schatten p-norm minimization. *Magn Reson Imaging* 2011;29:408–17.
- [33] Majumdar A, Ward RK, Aboulnasr T. Non-convex algorithm for sparse and low-rank recovery: application to dynamic MRI reconstruction. *Magn Reson Imaging* 2013;31:448–55.
- [34] Cao W, Sun J, Xu Z. Fast image deconvolution using closed-form thresholding formulas of regularization. *J Vis Commun Image R* 2013;24:31–41.
- [35] Dong B, Zhang Y. An efficient algorithm for l_0 minimization in wavelet frame based image restoration. *J Sci Comput* 2013;54:350–68.
- [36] Candès E, Wakin M, Boyd S. Enhancing sparsity by reweighted l_1 minimization. *J Fourier Anal App* 2008;14:877–905.
- [37] Baraniuk R, Choi H, Neelamani R, Ribeiro V, Romberg J, Guo H, Fernandes F, Hendricks B, Gopinath R, Lang M, Odegard JE, Wei D. Rice wavelet toolbox, <http://dsp.rice.edu/software/rice-wavelet-toolbox>, 2009.
- [38] Baker CA, King K, Liang D, Ying L. Translational-invariant dictionaries for compressed sensing in magnetic resonance imaging. In: Miles Wernick, editor. 8th IEEE International Symposium on Biomedical Imaging-ISBI'11. Chicago, USA: IEEE; 2011. p. 1602–5.
- [39] Vasanawala S, Murphy M, Alley M, Lai P, Keutzer K, Pauly J, Lustig M. Practical parallel imaging compressed sensing MRI: summary of two years of experience in accelerating body MRI of pediatric patients. In: Miles Wernick, editor. 8th IEEE International Symposium on Biomedical Imaging-ISBI'11. Chicago, USA: IEEE; 2011. p. 1039–43.
- [40] Hu C, Qu X, Guo D, Bao L, Chen Z. Wavelet-based edge correlation incorporated iterative reconstruction for undersampled MRI. *Magn Reson Imaging* 2011;29: 907–15.
- [41] Yang J, Zhang Y, Yin W. A fast alternating direction method for TV l_1 - l_2 signal reconstruction from partial fourier data. *IEEE J Sel Topics Signal Process* 2010;4: 288–97.
- [42] Chen Y, Ye X, Huang F. A novel method and fast algorithm for MR image reconstruction with significantly under-sampled data. *Inverse Probl Imag* 2010; 4:223–40.
- [43] Zhang Y, Dong B, Lu Z. l_0 minimization for wavelet frame based image restoration. *Math Comput* 2013;82:995–1015.
- [44] Wang Z, Bovik AC, Sheikh HR, Simoncelli EP. Image quality assessment: from error visibility to structural similarity. *IEEE Trans Image Process* 2004;13:600–12.
- [45] Bio Imaging Signal Processing Lab [Online]. Available: <http://bisip.kaist.ac.kr/kFOCUSS.htm>.
- [46] Puy G, Marques JP, Gruetter R, Thiran J, Van De Ville D, Vandergheynst P, Wiaux Y. Spread spectrum magnetic resonance imaging. *IEEE Trans Med Imaging* 2012;31:586–98.
- [47] Qu X, Chen Y, Zhuang Y, Yan Z, Guo D, Chen Z. Spread spectrum compressed sensing MRI using chirp radio frequency pulses, 2013, <http://arxiv.org/abs/1301.5451>.
- [48] Jacques L, Duval L, Chaux C, Peyre G. A panorama on multiscale geometric representations, intertwining spatial, directional and frequency selectivity. *Signal Process* 2011;91:2699–730.
- [49] Peyre G. A review of adaptive image representations. *IEEE J Sel Topics Signal Process* 2011;5:896–911.